Experimental investigation of the Peregrine Breather of gravity waves on finite water depth

G. Dong,[1] B. Liao,[1] Y. Ma,[1,*] and M. Perlin[2]

[1]*State Key Laboratory of Coastal and Offshore Engineering, Dalian University of Technology, Dalian 116023, China*

[2]*Ocean Engineering Department, Texas A&M University, College Station and Galveston, Texas 77554, USA*

(Received 15 November 2017; published 4 June 2018)

A series of laboratory experiments were performed to study the Peregrine Breather (PB) evolution in a wave flume of finite depth and deep water. Experimental cases were selected with water depths k_0h (k_0 is the wave number and h is the water depth) varying from 3.11 to 8.17 and initial steepness k_0a_0 (a_0 is the background wave amplitude) in the range 0.06 to 0.12, and the corresponding initial Ursell number in the range 0.03 to 0.061. Experimental results indicate that the water depth plays an important role in the formation of the extreme waves in finite depth; the maximum wave amplification of the PB packets is also strongly dependent on the initial Ursell number. For experimental cases with the initial Ursell number larger than 0.05, the maximum crest amplification can exceed three. If the initial Ursell number is nearly 0.05, a shorter propagation distance is needed for maximum amplification of the height in deeper water. A time-frequency analysis using the wavelet transform reveals that the energy of the higher harmonics is almost in-phase with the carrier wave. The contribution of the higher harmonics to the extreme wave is significant for the cases with initial Ursell number larger than 0.05 in water depth $k_0h <$ 5.0. Additionally, the experimental results are compared with computations based on both the nonlinear Schrödinger (NLS) equation and the Dysthe equation, both with a dissipation term. It is found that both models with a dissipation term can predict the maximum amplitude amplification of the primary waves. However, the Dysthe equation also can predict the group horizontal asymmetry.

DOI: 10.1103/PhysRevFluids.3.064801

I. INTRODUCTION

Freak waves, or rogue waves, which appear sporadically and subsequently disappear without a trace, can endanger ships and offshore structures due to their extraordinarily large wave heights [1–3]. Often a freak wave is identified as when its height exceeds twice the significant wave height [4–7]. Usually, occurrences of freak waves are reported following accidents and their wave heights are assessed by subsequent visual inspection. There have been a limited number of freak waves directly measured in the ocean. Over the past decades, much effort has been expended to reveal the generation mechanisms of freak waves. There are several possible physical mechanisms for generating freak waves [5,8]. In offshore regions, one of the most likely mechanisms is the modulational instability, which is related to four-wave interactions [9,10]. The modulational instability of gravity waves can be modeled well by the nonlinear Schrödinger (NLS) equations. Therefore, NLS-type equations often are used to study the characteristics of freak waves [11–13]. The Peregrine Breather (PB) is a

*yuxma@126.com

simple theoretical solution of the NLS equation. It predicts a double spatial-temporal localization, where the amplitude can reach three times its initial value. Therefore, it can be considered a model for freak waves [14]. Recently, physical experimental observations of PBs were reported in optics [15], in multicomponent plasmas [16], and in water waves [17]. Theoretically, there are higher-order breather solutions that are also localized in both space and time and have been observed experimentally for water waves [18,19] and for waves in fiber optics [20,21]. In addition, the PB has been exploited to study the impact of freak waves on marine structures by physical experiments [22,23] and via numerical simulations [24,25].

The experiments of Chabchoub *et al.* [17] on the evolution of PBs found that the experimental results agree well with the prediction by the NLS equation in deep water conditions ($k_0h \approx 11.6$, k_0 is the wave number and h is the water depth). In a shallower water depth condition ($k_0h \approx 7$), the experimental results of Shemer and Alperovich [26] found that the actual evolution of a PB deviates from the simulation using the NLS equation, but can be modeled better by the Dysthe equation [27]; it was also revealed that the bound higher-harmonics contribute significantly to the formation of the extreme waves. In reality, the occurrence of freak waves may appear in arbitrary depth [7]. Most importantly, however, the water depth k_0h of the recorded observations of freak waves is primarily in the range 1.5 to 5.0 [28–34]. Based on observations of freak waves in the ocean of intermediate depth, Didenkulova *et al.* [35] demonstrate that the modulational instability can still play a significant role in their formation for basins of large depth, and that the freak wave packet in a basin of intermediate depth lengthens and contains a larger number of individual waves rather than in deep water. Hu *et al.* [36] studied the PB evolution in deep water using a two-dimensional numerical wave model based on the incompressible N-S equations and found that the temporal span and the travel distance of PB between deep and finite water depth are quite different. Clauss *et al.* [37] presented an experimental study on the evolution of Kuznetsov-Ma breather solution [38,39] which has been applied to produce large amplitude waves in the seakeeping basin. It has been identified that the higher the initial steepness, the shorter the distances the wave train has to pass to reach the maximum wave height; the experiments also revealed that water depth influences the formation process significantly, and the distance the wave train has to pass to reach the maximum wave height increases significantly with decreasing water depth. Chabchoub *et al.* [40] experimentally confirmed the existence of the families of time-periodic first-order solutions of Kuznetsov-Ma breathers in water. The experiment complements the previous observation of the PB, which is a limiting case of the Kuznetsov-Ma solution when the periods go to infinity. Zhang *et al.* [41] performed a series of laboratory experiments in a seakeeping wave tank related to the Kuznetsov-Ma breather solution with different initial wave steepness and different lengths of carrier waves, and found that the generation of maximum wave height is generally accompanied by a very large wave crest. For the same dimensionless water depth, the maximum wave height and the growth rate are proportional to the initial wave steepness. Meanwhile, if the initial wave steepness of the breather solutions is the same, the distances that the groups are required to achieve the maximum wave crests decreased significantly as a function of the increase in water depth. They also found that the wave spectrum undergoes a significant change in the evolutionary process when an extreme wave is observed. Recently, Liao *et al.* [42] performed a series of laboratory experiments to study the evolution of PBs in a wave flume in finite depth, and wave trains were initially generated in a region of quiescent water and then propagated into an adverse current region for which the current velocity strength gradually increased from zero to an approximately stable value. The results show that in the presence of current the dynamics of the wave group are modified, the focusing point was shifted upstream, which indicated that the adverse current accelerates the evolution of the modulational instability, and the height of the extreme waves was increased.

Furthermore, previous studies also confirmed that bound higher harmonics could play an important role in the formation of freak waves [26]. According to the theory, the energy of the bound higher harmonics of a wave strongly depends on wave steepness and water depth. Hence, the propagation properties of PBs in different water depths are required, and the influence of water depth on the evolution of PBs is necessary. These are the motivation for the present study.

Following this Introduction, a brief background of the PB is introduced in Sec. II. The experimental setup is described in Sec. III. Then experimental results and discussion are presented in Sec. IV. Last, Sec. V presents the main conclusions.

II. THEORETICAL BACKGROUND

The NLS equation is known to capture accurately the weakly nonlinear evolution of narrow-band processes, and it is the simplest theoretical model describing the evolution of wave envelopes in arbitrary water depth. It takes the following form [43]:

$$i(A_t + c_g A_x) + \alpha A_{xx} + \beta |A|^2 A = 0, \tag{1}$$

where x and t denote the space coordinate and the time, respectively; A is the complex wave envelope; c_g is the group velocity; and the coefficients α and β are functions of the carrier wave angular frequency ω_0 and the water depth h, respectively, and can be expressed as

$$\alpha = -\frac{c_g^2}{2\omega_0} + \frac{\omega_0 h \cosh^2 k_0 h}{k_0 \sinh 2k_0 h} - h c_g \tanh k_0 h, \tag{2}$$

$$\beta = -\frac{\omega_0 k_0^2 (\cosh 4k_0 h + 8 - 2\tanh^2 k_0 h)}{16 \sinh^4 k_0 h} + \frac{\omega_0 (2\omega_0 \cosh^2 k_0 h + k_0 c_g)^2}{2\left(gh - c_g^2\right)\sinh^2 2k_0 h}, \tag{3}$$

where k_0 is the carrier wave number as determined by the linear dispersion relation. A dimensionless form of the NLS [44,45] is

$$i q_T + q_{XX} + 2|q|^2 q = 0, \tag{4}$$

which is obtained from Eq. (1) using the rescaled variables:

$$X = \frac{1}{2}\sqrt{\frac{2\beta}{\alpha}} a_0 (x - c_g t), \quad T = \frac{1}{2}\beta a_0^2 t, \quad q = \frac{A}{a_0}. \tag{5}$$

Here a_0 represents the initial wave amplitude of the background carrier wave. Peregrine [45] gave a first-order rational solution of the NLS equation, which has been called the Peregrine Breather (PB), and can be written as

$$q_p(X,T) = \left[1 - \frac{4(1+4iT)}{1+4X^2+16T^2}\right] \exp(2iT). \tag{6}$$

The PB is localized in both the space and time domains, and it can describe the main feature of freak waves, i.e., waves that appear from nowhere and disappear without a trace [14]. The dimensional form of the PB is

$$A(x,t) = a_0 \left[1 - \frac{4\left(1 + 2i\beta a_0^2 t\right)}{1 + 2\beta\alpha^{-1} a_0^2 (x - c_g t)^2 + 4\beta^2 a_0^4 t^2}\right] \exp\left(i\beta a_0^2 t\right). \tag{7}$$

Figure 1 presents an example of the solution with steepness $\varepsilon_0 = 0.104$ ($a_0 = 0.04$ m, $f_0 = 0.8$ Hz, $k_0 = 2.59$ m^{-1}, $\varepsilon_0 = k_0 a_0$ and $h = 1.2$ m). It is shown that the maximum amplitude of the PB is three times the background carrier wave: 0.12 m. The surface elevation, $\zeta(x,t)$, to leading order is

$$\zeta(x,t) = \mathrm{Re}\{A(x,t)\exp[i(k_0 x - \omega_0 t)]\}. \tag{8}$$

In the present study, Eq. (8) is used to determine the initial conditions for the motion of the wave maker. The position where the crest of the PB develops its maximum amplitude depends on the initial conditions input at the wave maker. To investigate the wave evolution to its maximum amplification and decrease the effect of reflected waves (that cannot be fully eliminated), the chosen position of maximum amplification should not be close to the end of the flume. The observation of the complete evolution of the breather starting from a slightly perturbed sinusoidal wave is not possible due to

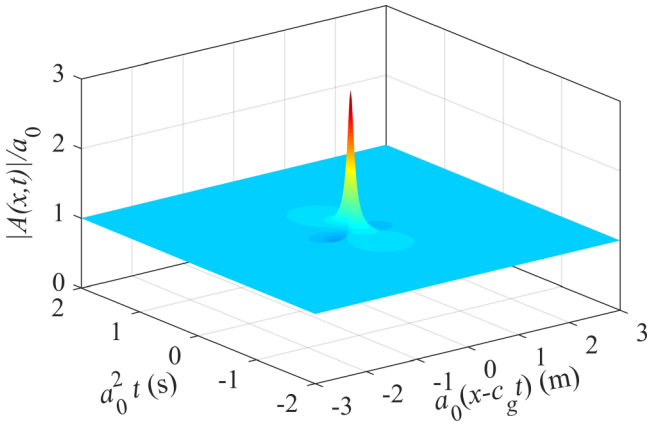

FIG. 1. Temporal and spatial evolution of the PB [Eq. (7)]. $a_0 = 0.04$ m, $f_0 = 0.8$ Hz, $k_0 = 2.59$ m^{-1}, $h = 1.2$ m.

the limited length of the flume. Therefore, to observe the occurrence of the breathers, the ratio of the relative height of the initial crest at the first location was adjusted to exceed about 1.6 times the background amplitude. Then the chosen location, x_0, of the maximum amplitude of the PB can be obtained theoretically. As is evident from Table I, it is clear that in the same water depth (e.g., $k_0h = 3.11$), the prescribed maximum location x_0 decreases with increasing wave steepness. Meanwhile, for a given steepness, a longer distance is needed to achieve the maximum amplification of wave amplitude in shallower water depth. However, as can be seen in Table I, the actual maximum crest location is always downstream of the prescribed location, which is mainly due to viscous dissipation (see the discussion in Sec. IV B). As discussed by Segur *et al.* [46] and Ma *et al.* [47], the presence of viscous dissipation can depress the growth rate of the modulational instability; therefore, it can cause the actual position of the maximum crest amplification to be beyond the theoretically predicted one. Figure 2 shows the expected location as a function of k_0h. The expected location decreases with an increase in k_0h. Meanwhile, a steeper wave train will reach the maximum amplification faster.

TABLE I. Wave parameters measured at the first location $x = 3.7$ m.

Case	f_0 [Hz]	a_0 [m]	$\varepsilon_0 = k_0a_0$	U_r	k_0h	x_0 [m]	x_m [m]	ΔE [%]	σ_e [m^{-1}]
1	0.8	0.025	0.065	0.033	3.11	94.9	–	20.71	0.0027
2	0.8	0.03	0.078	0.039	3.11	50.0	–	20.12	0.0029
3	0.8	0.04	0.104	0.052	3.11	32.3	39.2	26.53	0.0035
4	0.9	0.02	0.065	0.033	3.92	70.6	–	21.85	0.0028
5	0.9	0.03	0.098	0.049	3.92	30.1	33.2	23.88	0.0035
6	1.0	0.015	0.060	0.030	4.83	83.4	–	32.43	0.0036
7	1.0	0.02	0.081	0.040	4.83	45.8	–	28.77	0.0037
8	1.0	0.03	0.120	0.061	4.83	22.7	28.2	29.85	0.0037
9	1.2	0.015	0.087	0.044	6.96	28.7	29.2	31.23	0.0048
10	1.2	0.02	0.116	0.058	6.96	18.9	19.2	30.59	0.0046
11	1.3	0.015	0.102	0.051	8.17	19.3	21.2	33.61	0.0051

Note: x_0 and x_m are the prescribed maximum location and the measured maximum location, respectively; f_0: carrier wave frequency; a_0: background wave amplitude; ε_0: initial wave steepness; U_r: Ursell number; k_0h: relative water depth; – indicates that the maximum amplification did not occur in the present wave flume; ΔE: the total energy loss; σ_e: experimental dissipation rate.

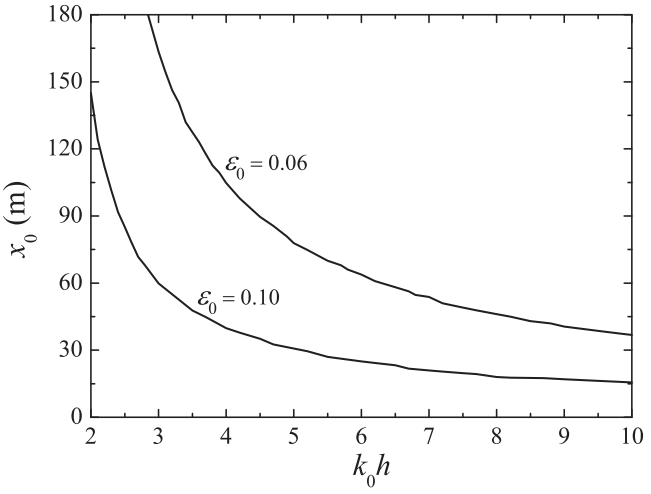

FIG. 2. The expected location as a function of $k_0 h$.

III. EXPERIMENTAL SETUP

Experiments were conducted in a wave flume located at the State Key Laboratory of Coastal and Offshore Engineering, Dalian University of Technology, Dalian, China. The flume is 69 m long, 2 m wide, and 1.8 m deep, and in this study, a water depth $h = 1.2$ m was used. The detailed experimental setup is shown in Fig. 3. The flume is equipped with a servo-motor-driven piston-type wave maker with $x = 0$ m defined as the mean position of the wave maker. To ensure two-dimensionality of the

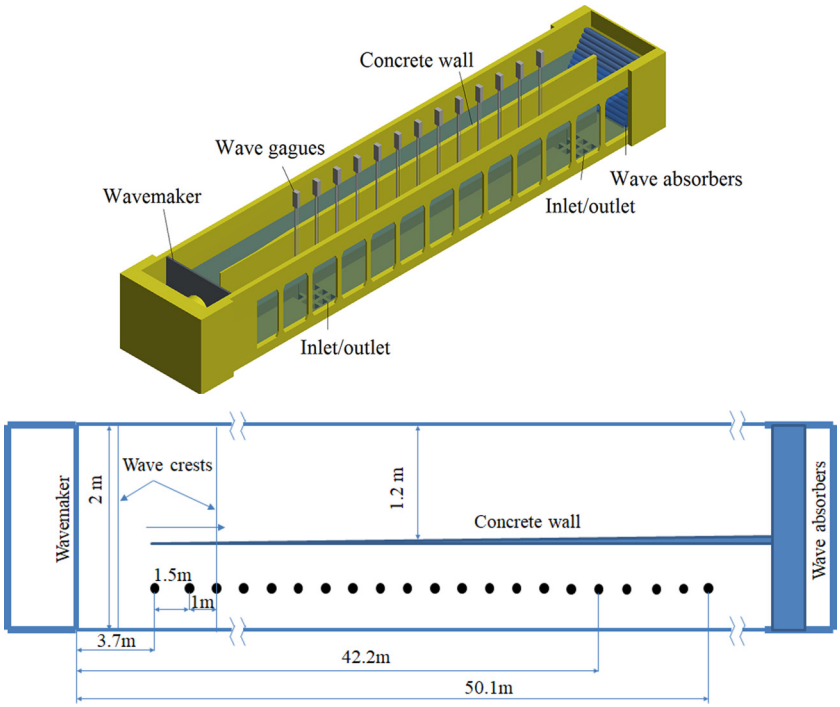

FIG. 3. Experimental setup (not to scale). Note that not all of the 46 wave probes are depicted in the sketch.

wave field, from $x = 3.2$ m onward, a surface-ground concrete wall (a roughness similar to the glass wall) is used to separate the flume longitudinally into two sections with widths of 0.8 m and 1.2 m. The narrower 0.8 m-wide channel is chosen as the working section. A wave absorber was installed at the opposite end to minimize wave reflections; prior experiments have shown that the reflection coefficient is only $\sim$5% for 1 Hz waves. The water elevations are simultaneously measured by 46 wave gauges positioned along the center line of the working section, some of which are shown by filled circles in Fig. 3. The first wave gauge is 3.7 m from the wave maker, and the measurements are performed in the range $3.7\ \text{m} \leqslant x \leqslant 50.1$ m. The wave maker is precisely controlled to generate the desired wave trains. The carrier wave parameters are determined by the background amplitude a_0 and the initial steepness ε_0. Chabchoub *et al.* [19] found that wave trains with $\varepsilon_0 > 0.12$ could evolve to breaking. Therefore, to avoid breaking the initial steepness of the present experiment is chosen to be less than 0.12 (0.06–0.12). To determine the water depth influence, the nondimensional water depths k_0h are varied from 3.11 to 8.17 by changing the carrier wave frequency. Water surface elevations are sampled with a frequency of 50 Hz, and the duration of each record is 163.84 s. It is noted that, as expected, no breaking is observed in the present experiments. The detailed wave parameters, which were determined from the measured data at the first location ($x = 3.7$ m), are shown in Table I. For some experimental cases, the locations where the maximum height amplification would have occurred are beyond the range of the present flume; therefore, they cannot be observed, as shown in the eighth column of Table I. Generalized Ursell number is another important parameter for measuring the nonlinearity of gravity waves, which is defined as [48,49]

$$U_r = \frac{a_0(3-\sigma^2)k_0}{4\sigma^3}, \tag{9}$$

where $\sigma = \tanh(k_0h)$. In shallow water, U_r is the ordinary Ursell number $3a_0/4k_0^2h^3$, while in deep water it is the wave slope $\frac{1}{2}k_0a_0$. The Ursell numbers are presented in Table I. As expected, for the same relative water depth k_0h and initial amplitude a_0, the U_r nearly half of the initial wave steepness ε_0. The generalized Ursell number is a representative nonlinearity parameter of gravity waves for all water depth, so we will use it in the following discussion.

IV. EXPERIMENTAL RESULTS AND DISCUSSION

A. Evolution of surface elevations

The measured surface elevations of experimental Case 3 ($U_r = 0.052$) at 12 selected locations along the flume are shown in Fig. 4. The initial wave packet consists of about 50 waves and is initially close to a sinusoidal wave train except for the perturbation in the middle. An extremely large wave is observed growing in the propagation direction from this localized perturbation. Close to where the maximum crest is seen, the rate of the amplitude growth is accelerated. The maximum crest appeared at $x = 39.2$ m and reached 0.151 m, with an amplification factor about 3.78, which significantly exceeds three. (As mentioned previously, no breaking is seen.) Subsequently, the maximum amplitude decays downstream. The dashed lines in Fig. 4 originate at the center of the initial wave train and correspond to the location of the point propagating with the linear group velocity $c_g = 0.995\ \text{m s}^{-1}$ and the third-order nonlinear group velocity $c_g = 1.012\ \text{m s}^{-1}$ [50], respectively. Due to dispersion and the nonlinear effects, the propagation velocity of the steepest crest exceeds the linear group velocity c_g, which is in agreement with the previous experimental observations and the numerical simulations [26,51,52]. The average speed of the maximum crest between 39.2 m and 45.1 m was about $1.34\ \text{m s}^{-1}$, which is significantly larger than the theoretical predictions. This may be caused by the frequency modulation and the rapid exchange of energy among free waves in the wave packet (as discussed below). Figure 5 presents the wave elevations measured at twelve locations for Case 8 that is in deeper water. The evolution trend of this case is similar to that of Case 3. At the focal location, the maximum crest reached 0.097 m, with an amplification factor about 3.23 of the initial carrier wave. It is interesting to notice that, even though the initial steepness of Case 8 is larger than

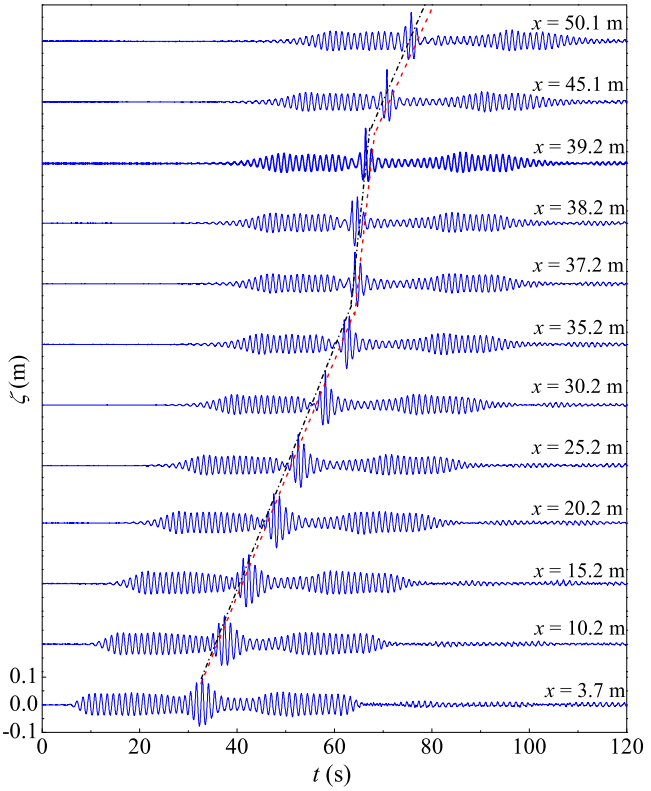

FIG. 4. Temporal evolution of the surface elevations at 12 different locations along the flume (Case 3: $k_0h = 3.11$, $U_r = 0.052$). Dashed red and dashed dot black lines correspond to propagation with the linear group velocity $c_g = 0.995$ m s^{-1} and the third-order nonlinear group velocity $c_g = 1.012$ m s^{-1}, respectively.

Case 3, the amplification factor of the case in deeper water is smaller than that of the shallower one, suggesting that the water depth plays an important role in the formation of the extreme waves.

Figure 6 shows a comparison of the theoretical prediction by Eq. (8) at the first gauge ($x = 3.7$ m) and the position of maximum amplitude with the measured surface elevation at the position where the maximum amplitude amplification was achieved (it should be noted that the measured results are shifted to assure that the two maximum crests are in phase). At the first location, the experimental results agree well with the theoretical results; however, at the maximum amplification positions, besides the left-right asymmetry of the wave group, the measured maximum wave crest was almost 26% and 7.4% higher than the theoretical predications for Case 3 and Case 8, respectively. The discrepancy between the surface elevations of the measurement and the prediction is more obvious for the shallower case. The wave amplitude spectra obtained by FFT at various locations along the flume are presented in Figs. 7 and 8. All wave spectra exhibit a typical triangular spectrum colocated with the main frequency component of the background wave. If the Ursell number, U_r, was smaller than 0.05 [e.g., Figs. 7(a)–7(c)], the change to the wave spectrum is not obvious in the evolutionary process. However, if the Ursell number was larger than 0.05 [e.g., Fig. 7(d) and Figs. 8(b)–8(d)], the wave spectrum underwent a significant change. The magnitudes of the upper side frequency bands of the carrier waves increased rapidly prior to the location where the extremely large wave was observed; the spectrum widened and developed visible left-right asymmetry. The high-order harmonics can be identified and become increasingly essential in the process of spatial evolution. Farther downstream, the corresponding large wave decayed rapidly, and the part of the upper sides'

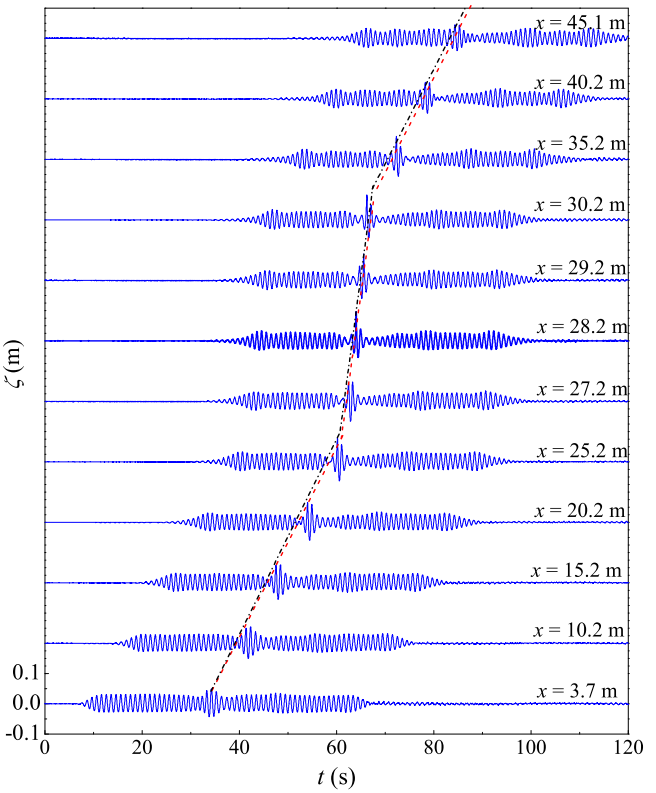

FIG. 5. Temporal evolution of the surface elevations at 12 different locations along the flume (Case 8: $k_0h = 4.83$, $U_r = 0.061$). Dashed red and dashed dot black lines correspond to propagation with the linear group velocity $c_g = 0.781$ m s^{-1} and the third-order nonlinear group velocity $c_g = 0.798$ m s^{-1}, respectively.

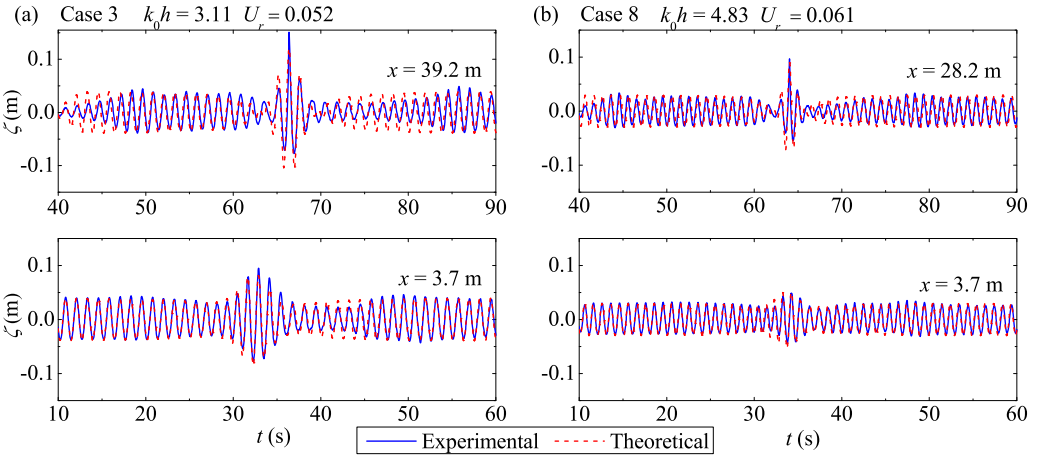

FIG. 6. Comparison of the measured surface height at the first gauge ($x = 3.7$ m) and the position of maximum wave amplitude with the theoretical PB solution for (a) Case 3; (b) Case 8. (These wave trains have been shifted in time so that the maximum peaks are shown to occur simultaneously.)

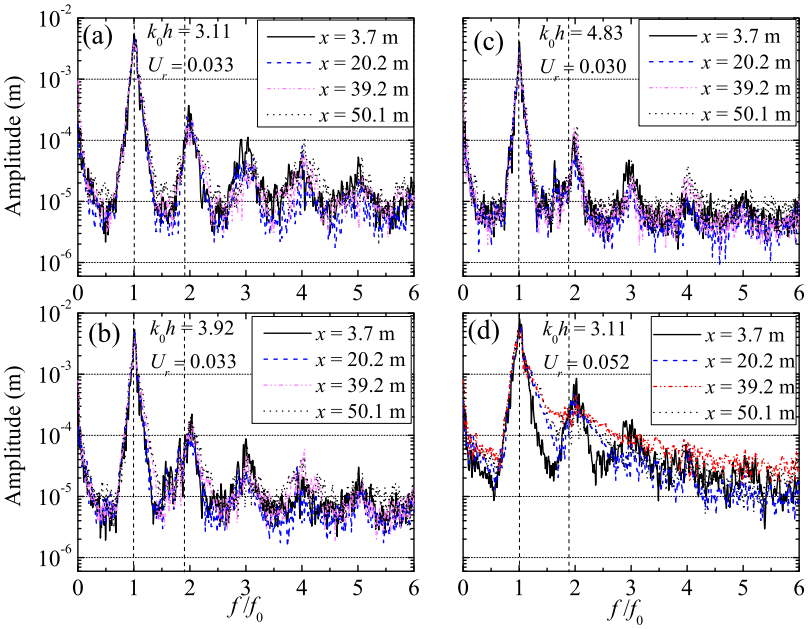

FIG. 7. The wave amplitude spectra at various locations along the flume. The vertical dashed lines represent the boundaries of the frequency range (f_0, 1.8f_0), the red dash dotted lines denote the spectra of the maximum wave in the evolutionary process. (a) Case 1; (b) Case 4; (c) Case 6; (d) Case 3.

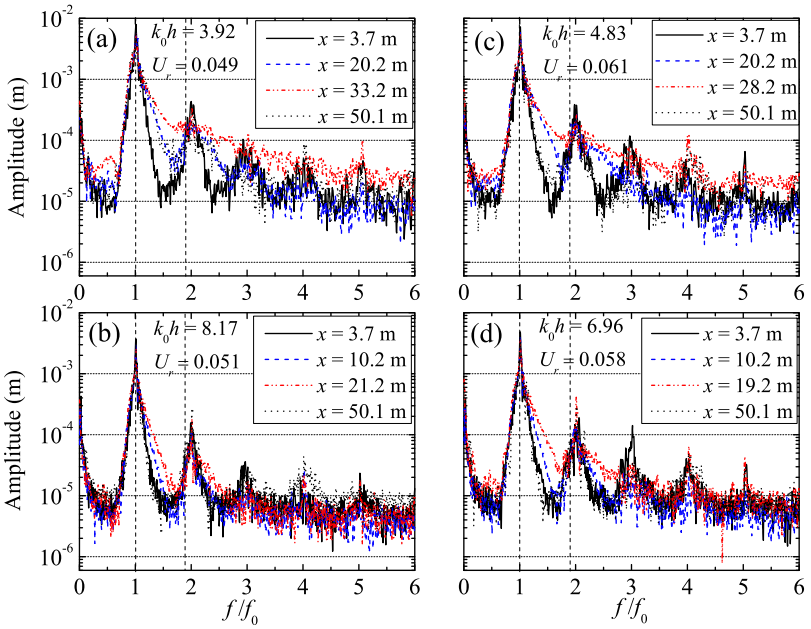

FIG. 8. The wave amplitude spectra at various locations along the flume. The vertical dashed lines represent the boundaries of the frequency range (f_0, 1.8f_0), the red dash dotted lines denote the spectra of the maximum wave in the evolutionary process. (a) Case 5; (b) Case 11; (c) Case 8; (d) Case 10.

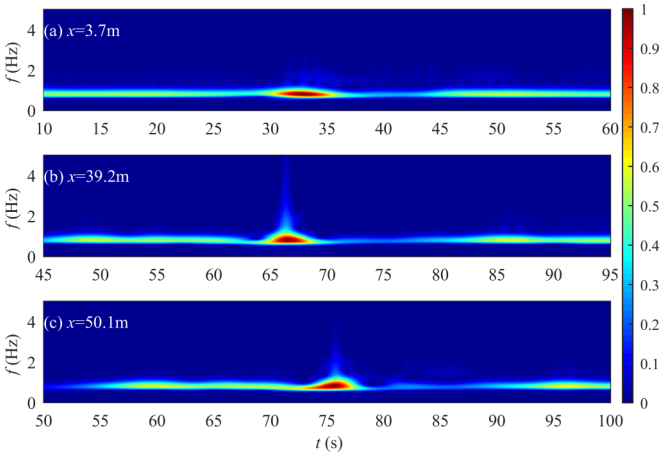

FIG. 9. The corresponding wavelet spectrum of Case 3 at three locations: (a) $x = 3.7$ m; (b) $x = 39.2$ m; (c) $x = 50.1$ m. (Each spectrum is nondimensionalized by the maximum value at each location.)

energy transferred back to the lower frequency component, and the width of the spectrum seemed to decrease, indicating that the nonlinear energy transfer was somewhat reversible, especially in deeper water conditions. Similar variations were observed by Shemer and Alperovich [26] and Zhang *et al.* [41].

The above wave amplitude spectral analysis shows only the change in the frequency spreading during the evolution, and that the energy of the higher harmonics was relatively small. As shown in the previous section, the surface elevations of the maximum waves were strongly asymmetric, indicating that the energy of the higher harmonics will be substantial at that instant in time. To ascertain the contribution of the higher harmonics, time-frequency analysis is needed. The wavelet transform analysis is more appropriate to analyze the time series and examine the localized freak wave characteristics in the time-frequency domain [28,53]. Hence, an analysis of the extreme waves was conducted via the wavelet analysis. In the present study, the Morlet wavelet was selected as the mother wavelet. Figures 9 and 10 display the wavelet spectra of Case 3 and Case 11 at the three different locations. It is noted that the wavelet spectrum was nondimensionlized by the maximum wavelet energy at each location. At the locations far from the focal position, the majority of wave energy

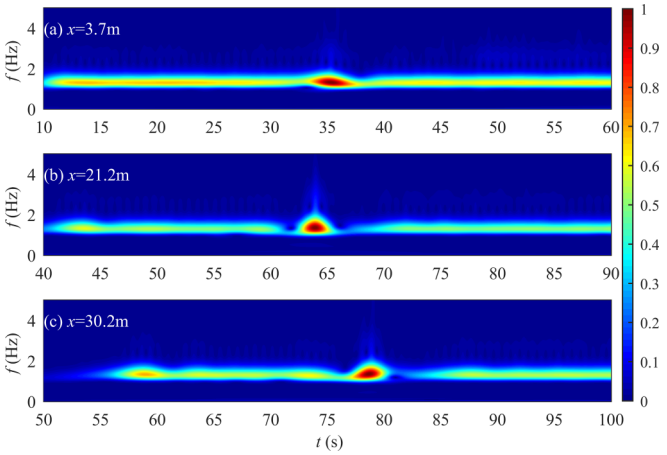

FIG. 10. The corresponding wavelet spectrum of Case 11 at three locations: (a) $x = 3.7$ m; (b) $x = 21.2$ m; (c) $x = 30.2$ m. (Each spectrum is nondimensionalized by the maximum value at each location.)

was distributed around the center frequency of the carrier wave, but the instantaneous frequency of the wave packet in the middle of the wave train demonstrates a down-chirped type signal, i.e., the instantaneous frequency decreases with time [e.g., Fig. 9(a): $t \in$(30 s, 35 s); Fig. 10(a): $t \in$(33 s, 38 s)]. At the instantaneous time of the maximum height, the frequency components seem to in phase approximately [e.g., Fig. 9(b): $t \in$(65 s, 70 s); Fig. 10(b): $t \in$(61 s, 66 s)], and the energy of the higher harmonics becomes significant, resulting in a widening spectrum for a brief period. At the downstream location, however, the instantaneous frequency demonstrates an up-chirp type signal [e.g., Fig. 9(c): $t \in$(73 s, 78 s); Fig. 10(c): $t \in$(76 s, 81 s)]. A similar trend of the wave group development with distance was observed experimentally and numerically by Kharif *et al.* [54], but the wave groups in their study were initially dispersive focusing. Furthermore, the instantaneous increase of the higher-harmonics for the case with the deeper water depth (Case 11) is less obvious than the shallower case, again indicating that the contribution of the higher-order harmonics to generate freak waves depends on water depth.

The spatial variation of the nondimensionalized maximum wave crest and the nondimensionalized maximum wave height of the cases are presented in Fig. 11. For example, the maximum amplification of the wave height ($H_{\max}/2a_0$) for the experimental Case 3 ($k_0h = 3.11$, $U_r = 0.052$) was 2.86, where H was defined as the vertical distance between the maximum wave crest and the rear trough. Additionally, the maximum value of $\zeta_{\max}/a_0$ was 3.78. The result once again demonstrates the vertical asymmetry of a wave profile when a large wave was observed. It is clear that the major feature of the PB is that its maximum wave crest and maximum wave height are reached at a single point and then decay from the region of localization, consistent with the theoretical predication. The spatial variation of the nondimensionalized wave crest exhibits significant fluctuations in the spatial region in proximity to the maximum amplification. It seems that the fluctuation was related closely to the initial Ursell number and the water depth. The fluctuations of the cases with smaller initial Ursell number were not as distinct. A comparison of the crest and the wave height variations finds that the fluctuation of the wave height was not as obvious as that of the crest, indicating strong vertical asymmetry of the surface elevations during the formation of extreme events. According to the theory, the PB is caused by the modulational instability of waves. However, the observations in the present experiment suggest that the higher-order harmonics also play an important role in the formation of the extreme events as follows.

To eliminate the contribution of the higher-order harmonics, the recorded signals were band-pass filtered in the range $0.6f_0 < f < 1.8f_0$ (based on the spectral analysis; Figs. 7 and 8). Figures 11(a)–11(e) show the wave crests of the filtered results (open symbols denote the filtered recording, and the solid symbols denote the original data). At the same water depth, the discrepancies between the filtered and the nonfiltered measurements increase with increasing Ursell number. For the cases with smaller steepness, the contribution of the higher harmonics to the maximum wave crest and the wave height is negligible. Additionally, the higher harmonics with larger Ursell number have a greater contribution to the maximum wave crest and the height. The contribution of the higher-order harmonics decreases as a function of increasing water depth. On the other hand, if the initial Ursell number was close [e.g., Fig. 11(a) (Case 3) and Fig. 11(e) (Case 11): $U_r = 0.052$ and 0.051; Fig. 11(c) (Case 8) and Fig. 11(d) (Case 10): $U_r = 0.061$ and 0.058], the distances that the groups required to achieve the maximum wave crests decreased significantly as a function of the increase in water depth. This is consistent with the theoretical predication as the growth rate of the modulational instability increases with increasing water depth [55–57]. Similar results were experimental found also by Clauss *et al.* [37] and Zhang *et al.* [41].

B. Comparison between the experiments and numerical results

The evolution of PBs is usually studied using the NLS equation or a modified NLS equation [14,24,26,45]. The rational multibreathers solutions from the first to the fifth order of the NLS are found in numerical simulations of the Dysthe equation by Slunyaev *et al.* [58]. The exact solutions of the NLS equation are reproduced by Ref. [58], which found that the NLS equation provided good

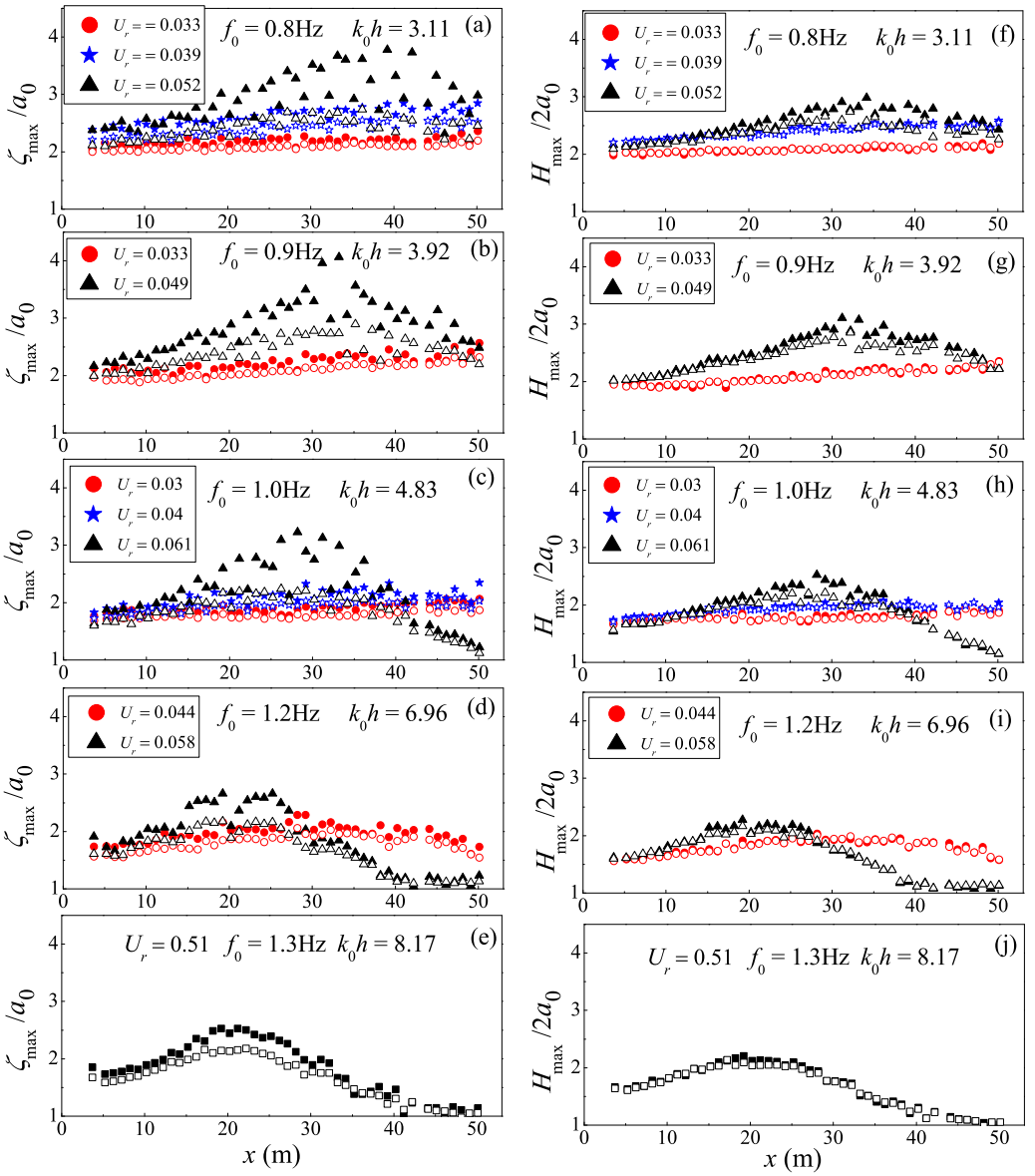

FIG. 11. Spatial variation of maximum wave crest (left) and maximum wave height (right) in the cases (Cases 1 through 11 shown via U_r) with different wave steepness and relative water depth; hollow symbols denote the filtered recording, and the solid symbols denote the original data.

qualitative evolution of the point of maximum in the case of the PB but predicts its appearance earlier than it happens in the Dysthe model; meanwhile, the effect of bound wave components is found to be very important in the evolution process. In the present study, the NLS equation [59] and the Dysthe equation [47] are used for comparison with the experimental data, and further to assess the ability of the two models to predict the PB evolution in the present experiments. Even without wave breaking, wave energy dissipation cannot be avoided in a physical wave flume. Experimental studies [46,47] showed that dissipation can weaken or even prevent the development of the modulational instability. In the present experiments, the energy dissipation is obvious for all the cases along the wave flume

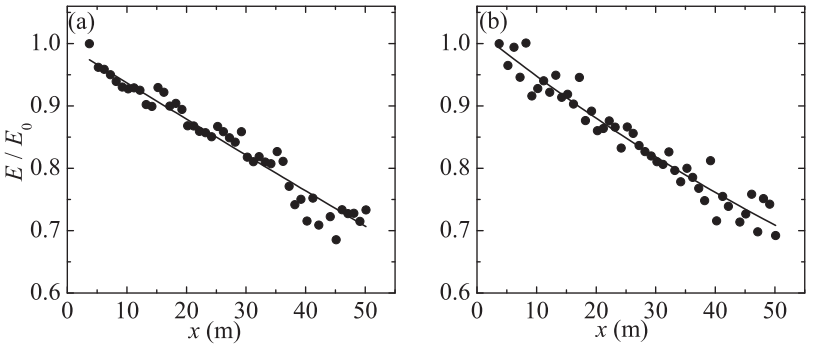

FIG. 12. The measured $E/E(0)$ and the fitted curves [Eq. (12)] versus the distances from the wave maker: (a) Case 3; (b) Case 8.

(see the last two columns in Table I). Therefore, to simulate the PB evolution properly using the models, a linear damping term should be and is added [46].

The total energy dissipation (presented as a percentage in Table I) in the measurement range, 3.7 m $< x <$ 50.1 m, is estimated as

$$\Delta E = (E_i - E_f)/E_i, \tag{10}$$

where E_i and E_f are the energy at the first ($x = 3.7$ m) and last ($x = 50.1$ m) measurement locations, while the wave energy E is defined as

$$E = \sum_{n=t_1}^{t_2} \zeta_n^2, \tag{11}$$

where t_1 and t_2 are the beginning and ending times of the breather wave trains, and ζ_n is the free surface elevation. It is assumed that the wave energy decay is exponential [46,47,60]:

$$E(x) = E(0)\exp(-2\sigma_e x), \tag{12}$$

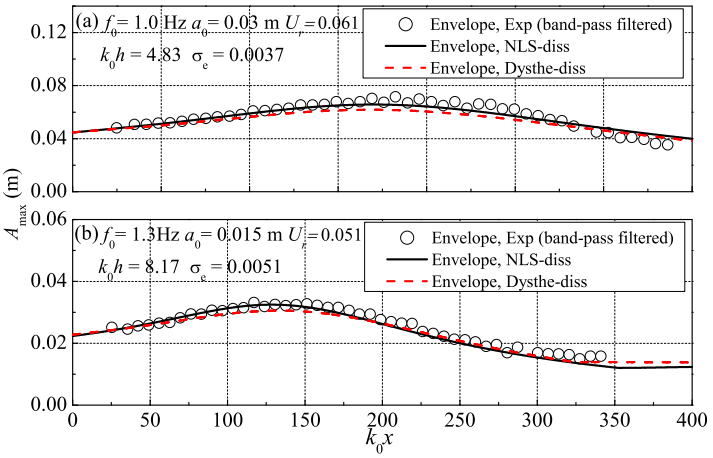

FIG. 13. Calculated [NLS and Dysthe equations with the dissipation term, the surface elevations $\zeta(x,t)$ are related to the variable $A(x,t)$ to the leading order] and measured maxima of the absolute values of the wave train envelope of the series (band-pass filtered [$0.6f_0$, $1.8f_0$]): (a) Case 8; (b) Case 11.

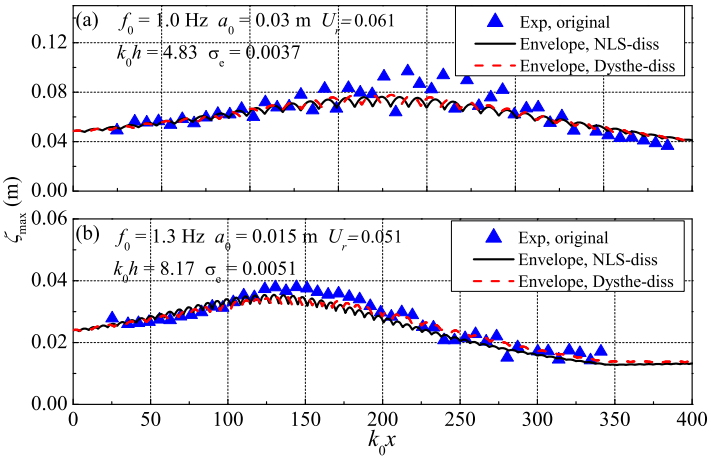

FIG. 14. The variations of the maximum crests along the propagation direction for the selected cases (a) Case 8; (b) Case 11. The results obtained by the numerical models are corrected to the third Stokes order.

where $E(0)$ is the energy at the first location. The measured data are fitted using the least-squares method to obtain the dissipation rate σ_e. The last column of Table I presents the fitted decay parameter σ_e for each case. Figure 12 illustrates the fitted curves for two experimental cases. It is clear that the normalized wave energy decay can be described reasonably well by the exponential curves along the flume.

Using the fitted value of σ_e the linear damping term is added in the NLS equation and the Dysthe equation in the way adopted by Ma *et al.* [47]. Then the equations are solved using

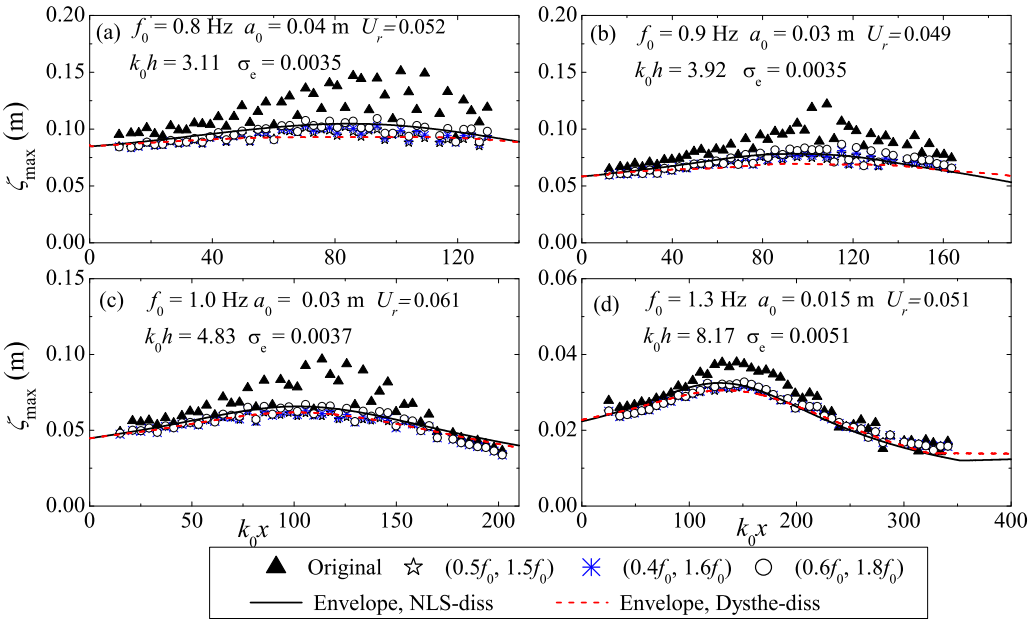

FIG. 15. The variations of the maximum crests along the propagation direction for the selected cases (a) Case 3; (b) Case 5; (c) Case 8; (d) Case 11. The results obtained by the numerical models are corrected to the leading Stokes order.

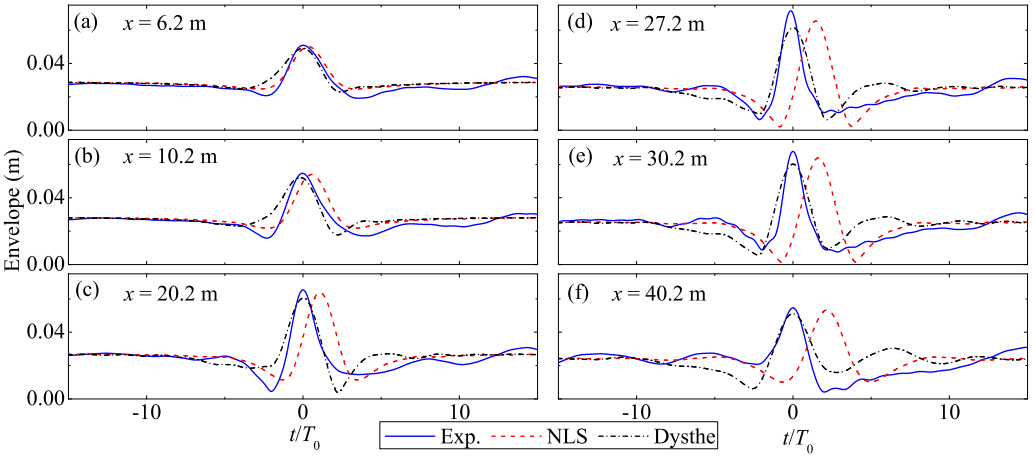

FIG. 16. Comparison of the computed and measured experimental shapes (band-pass filtered $[0.6f_0, 1.8f_0]$) of the modulus of the complex wave train envelope for Case 8: $U_r = 0.061$, $k_0h = 4.83$.

the split-step method proposed by Lo and Mei [61]. Figure 13 shows the comparison between the maximum envelope obtained directly by the NLS and Dysthe equations with a dissipation term from the experimental results. These are obtained from the Hilbert transform of the band-pass filtered $[0.6f_0, 1.8f_0]$ series, along the propagation direction for Case 8 and Case 11. The other cases give the similar results; therefore, they are not presented herein. Clearly, both models reflect the variations of the maximum values of the envelopes. The calculated envelopes can be converted to surface elevations (corrected to the Stokes third order) using the method provided by Lo and Mei [61]. Figure 14 shows the variations of the maximum crest obtained by the experiments and the NLS and the Dysthe equations' predictions along the propagation direction for Case 8 and Case 11. It is found that both numerical models can well describe the results at the upstream and downstream locations far from the maximum amplitude amplification. However, in the region close to the maximum amplification, the numerical model predictions are clearly lower than the experimental data, indicating that the harmonics that are higher than the third order contribute to the formation of the extreme events. Additionally, the discrepancy in shallower water is more distinct than the case in deeper water, suggesting the contribution of higher harmonics in shallower water is more significant.

In order to analyze the reasons of produce errors between the experiments and the numerical results in Fig. 14, we conducted a sensitivity analysis on the filtering range of the waves. According to the spectral analysis (Figs. 7 and 8), three filtering ranges for the experimental cases were selected: $[0.5f_0, 1.5f_0]$, $[0.4f_0, 1.6f_0]$, and $[0.6f_0, 1.8f_0]$. The results can be seen in Fig. 15. For the experimental

TABLE II. The maximum amplification of the surface elevation of measured and calculated with the NLS and Dysthe equations, with (labeled -diss) and without dissipation. The data are band-pass filtered in the range $[0.6f_0, 1.8f_0]$.

Case	k_0h	Exp.	Exp. (filtered)	NLS	NLS-diss	Dysthe	Dysthe-diss
3	3.11	3.78	2.74	3.213	2.180	3.155	2.253
5	3.92	4.06	2.89	3.211	2.366	3.158	2.559
8	4.83	3.23	2.24	3.253	2.543	3.131	2.593
9	6.96	2.29	2.06	3.220	2.264	3.022	2.256
10	6.96	2.66	2.18	3.230	2.350	3.116	2.344
11	8.17	2.53	2.18	3.104	2.362	3.071	2.308

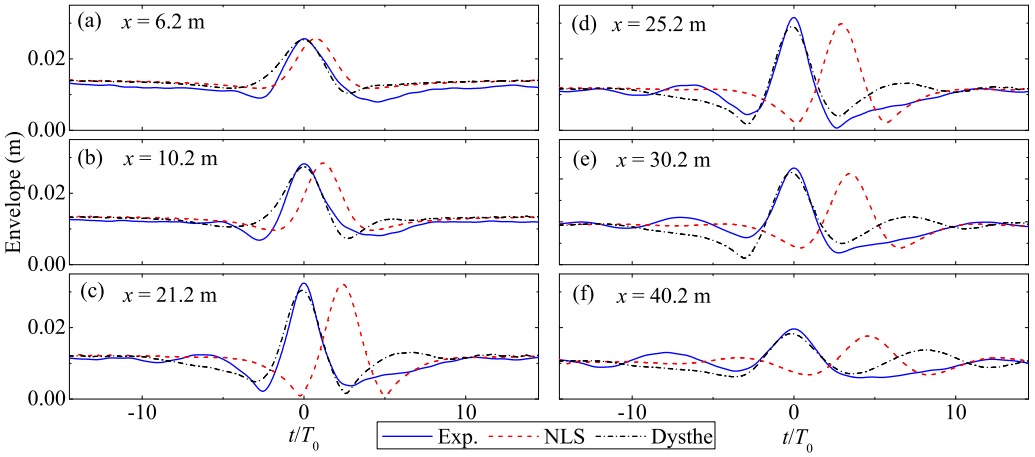

FIG. 17. Comparison of the computed and measured experimental shapes (band-pass filtered $[0.6\,f_0, 1.8\,f_0]$) of the modulus of the complex wave train envelope for Case 11: $U_r = 0.051$, $k_0h = 8.17$.

cases with water depth $k_0h < 5$, the deviations among the results obtained using the three different filtering ranges are obvious, especially in the region close to the maximum amplification. However, for the cases in deeper water, $k_0h > 5$, the difference is much smaller. And Fig. 15 also shows the comparison between the maximum envelope obtained directly by the NLS and Dysthe equations with a dissipation term from the linearization experimental results (the filtering of bound waves). It is found that the NLS equation compares reasonably well with the linearization experimental results in all cases, while the Dysthe equation performs better in deeper water depth. As can be seen in Fig. 15, difference filtering ranges do produce divergence of the maximum envelope close to the maximum amplification. For the experimental cases with water depth $k_0h < 5$, the deviations among the results obtained using the three different filtering ranges are obvious. For the cases in deeper water, $k_0h > 5$, the difference is much smaller. However, all the filtered results fit reasonably well with the numerical results by the NLS and Dysthe equations. Hence, the difference between the numerical and the experimental results is mainly due to the higher harmonics. Table II shows the maximum amplitude amplifications in the experiment and in the NLS and Dysthe equations with and without the dissipation term. The NLS and Dysthe equations give similar results. However, for $k_0h < 5$, the experimental results are much larger than the predictions. The discrepancy is much smaller in deeper water.

Comparisons between the envelopes of the wave trains of the primary waves along the flume for the two experimental cases are shown in Figs. 16 and 17. The envelope shapes predicted by the NLS equations are always symmetric with respect to the maximum amplitude, whereas the Dysthe equation compares reasonably well with the experimental results, exhibiting clear horizonal asymmetry. Due to the linear group velocity assumption, it is found also that the results of the NLS equation gradually lag further behind the experimental results as well as the Dysthe equation prediction. Similar results were also found by Shemer and Alperovich [26].

V. CONCLUDING REMARKS

The Peregrine Breather (PB) is a rational solution of the nonlinear Schrödinger (NLS) equation and is localized in both space and time; it culminates in an amplification of three times the initial wave amplitude. Therefore, it is often considered an appropriate model of freak waves in the ocean. In the present study, a series of laboratory experiments are performed to study the PB evolution in a wave flume in finite depth and in deep water; the nondimensional water depths k_0h are varied from 3.11 to 8.17 while the initial steepness of the present experiments is chosen from 0.06 to 0.12, and

the corresponding initial Ursell number in the range of 0.03 to 0.61. The experimental data show that the maximum wave amplification is dependent strongly on the initial Ursell number and the water depth. If the initial Ursell number larger than 0.05, the maximum crest amplification can exceed three. For the cases with nearly initial Ursell number 0.05, the distance that the group has to travel to achieve its maximum wave height will decrease significantly as the water depth increases. The results indicate that the water depth plays an important role in the formation of the extreme waves in finite water depth. The spectral bandwidth of the experimental cases with large Ursell number is broader during the formation of extreme waves and then becomes narrower. The spectral bandwidth can be nearly reversed if the effective propagation distance is sufficiently long. The time-frequency energy distribution in the abnormally large wave is examined also by the wavelet transform. It is found that the energy of the higher harmonics is almost in-phase with the carrier wave and contributes significantly to formation of the extreme events, especially for wave trains with initial Ursell number larger than 0.05. The contribution of the higher harmonics to the formation of the extreme events is significant for the cases with initial Ursell number larger than 0.05 in water depth $k_0h < 5$. The NLS equation and the Dysthe equation are also employed to simulate the wave evolution of the experimental cases. A linear damping term is added in the models from a fit of the experimental measurements, i.e., the dissipation rates of each case are estimated from the experimental data using a least square method. It is found that both models can predict well the evolution of the primary waves. However, the Dysthe equation performs better in simulating the shape variations of the wave groups, i.e., the horizontal asymmetry between the front and rear of the envelopes.

ACKNOWLEDGMENTS

This research is supported financially by the National Natural Science Foundation of China (Grants No. 51679031, No. 51720105010, and No. 51422901), High-Tech Ship Research Projects Sponsored by the Ministry of Industry and Information Technology (MIIT) of China (Grant No. 2016-23-7), and the Fundamental Research Funds for the Central Universities (Grant No. DUT16TD08).

[1] I. V. Lavrenov, *Wind Waves in Ocean: Dynamics and Numerical Simulations* (Springer-Verlag, Heidelberg, 2003).

[2] A. Lechuga, Were freak waves involved in the sinking of the tanker "Prestige"? Nat. Hazards Earth Syst. Sci. **6**, 973 (2006).

[3] K. B. Dysthe, H. E. Krogstad, and P. Muller, Oceanic rogue waves, Annu. Rev. Fluid Mech. **40**, 287 (2008).

[4] P. Klinting and S. Sand, Analysis of prototype freak waves, *Proceedings in Coastal Hydrodynamics*, edited by R. A. Dalrymple, Vol. 618 (University of Delaware, Newark, 1987).

[5] C. Kharif and E. Pelinovsky, Physical mechanisms of the rogue wave phenomenon, Eur. J. Mech. B **22**, 603 (2003).

[6] N. Mori, Occurrence probability of freak wave in nonlinear wave field, Ocean Eng. **31**, 165 (2004).

[7] C. Kharif, E. Pelinovsky, and A. Slyunyaev, *Rogue Waves in the Ocean* (Springer, Berlin, 2009).

[8] I. V. Lavrenov, The wave energy concentration at the Agulhas Current of South Africa, Nat. Haz. **17**, 117 (1998).

[9] T. B. Benjamin and J. E. Feir, The disintegration of wave trains on deep water, Part 1. Theory, J. Fluid Mech. **27**, 417 (1967).

[10] P. A. E. M. Janssen, Nonlinear four wave interaction and freak waves, J. Phys. Oceanogr. **33**, 863 (2003).

[11] A. R. Osborne, M. Onorato, and M. Serio, The nonlinear dynamics of rogue waves and holes in deep-water gravity wave train, Phys. Lett. A **275**, 386 (2000).

[12] M. Onorato, A. R. Osborne, M. Serio, and S. Bertone, Freak Wave in Random Oceanic Sea States, Phys. Rev. Lett. **86**, 5831 (2001).

[13] A. Chabchoub, N. Akhmediev, and N. P. Hoffmann, Experimental study of spatiotemporally localized surface gravity water waves, Phys. Rev. E **86**, 016311 (2012).

[14] V. I. Shrira and V. V. Geogjaev, What makes the Peregrine soliton so special as a prototype of freak waves? J. Eng. Math. **67**, 11 (2010).
[15] B. Kibler, J. Fatome, C. Finot, G. Millot, F. Dias, G. Genty, N. Akhmediev, and J. M. Dudley, The Peregrine soliton in nonlinear fibre optics, Nat. Phys. **6**, 790 (2010).
[16] H. Bailung, S. K. Sharma, and Y. Nakamura, Observation of Peregrine Solitons in a Multicomponent Plasma with Negative Ions, Phys. Rev. Lett. **107**, 255005 (2011).
[17] A. Chabchoub, N. P. Hoffmann, and N. Akhmediev, Rogue Wave Observation in a Water Wave Tank, Phys. Rev. Lett. **106**, 204502 (2011).
[18] A. Chabchoub, N. P. Hoffmann, and N. Akhmediev, Super Rogue Waves: Observation of a Higher-Order Breather in Water Waves, Phys. Rev. X **2**, 011015 (2012).
[19] A. Chabchoub, N. P. Hoffmann, M. Onorato, A. Slunyaev, A. Sergeeva, E. Pelinovsky, and N. Akhmediev, Observation of a hierarchy of up to fifth-order rogue wave in a water tank, Phys. Rev. E **86**, 056601 (2012).
[20] B. Frisquet, B. Kibler, and G. Millot, Collision of Akhmediev Breathers in Nonlinear Fiber Optics, Phys. Rev. X **3**, 041032 (2013).
[21] B. Frisquet, A. Chabchoub, J. Fatome, C. Finot, B. Kibler, and G. Millot, Two-stage linear nonlinear shaping of an optical frequency comb as rogue nonlinear-Schrödinger-equation solution generator, Phys. Rev. A **89**, 023821 (2014).
[22] M. Onorato, D. Proment, G. Clauss, and M. Klein, Rogue waves: From nonlinear Schrödinger breather solutions to sea-keeping test, PLoS ONE **8**, e54629 (2013).
[23] Y. Deng, J. Yang, X. Tian, and X. Li, Experimental investigation on rogue waves and their impacts on a vertical cylinder using the Peregrine breather model, Ships Offshore Struct. **11**, 757 (2016).
[24] W. Lu, J. Yang, and X. Tian, Fourth-order split-step pseudo-spectral method for the modified nonlinear Schrödinger equation, Ships Offshore Struct. **12**, 424 (2017).
[25] W. Lu, J. Yang, and S. Fu, Numerical study of the generation and evolution of breather-type rogue waves, Ships Offshore Struct. **12**, 66 (2013).
[26] L. Shemer and L. Alperovich, Peregrine breather revisited, Phys. Fluids. **25**, 051701 (2013).
[27] K. B. Dysthe, Note on the modification of the nonlinear Schrödinger equation for application to deep water waves, Proc. R. Soc. London A **369**, 105 (1979).
[28] N. Mori, P. C. Liu, and T. Yasuda, Analysis of freak wave measurements in the Sea of Japan, Ocean Eng. **29**, 1399 (2002).
[29] M. Paprota, J. Przewlocki, W. Sulisz, and B. E. Swerpel, Extreme waves and wave events in the Baltic Sea, in *Rogue Waves: Forecast and Impact on Marine Structures* (GKSS Research Center, Geesthacht, Germany, 2003).
[30] D. A. G. Walker, P. H. Taylor, and R. E. Taylor, The shape of large surface waves on the open sea and the Draupner New Year wave, Appl. Ocean Res. **26**, 73 (2004).
[31] P. Stansell, Distributions of freak wave heights measured in the North Sea, Appl. Ocean Res. **26**, 35 (2004).
[32] Z. Cherneva and C. G. Soares, Non-linearity and non-stationarity of the new year abnormal wave, Appl. Ocean Res. **30**, 215 (2008).
[33] A. Magnusson and M. Donelan, The Andrea wave characteristics of a measured North Sea rogue wave, J. Offshore Mech. Arct. Eng. **135**, 031108 (2013).
[34] F. Fedele, J. Brennan, S. P. de León, J. Dudley, and F. Dias, Real world ocean rogue waves explained without the modulational instability, Sci. Rep. **6**, 27715 (2016).
[35] I. I. Didenkulova, I. F. Nikolkina, and E. N. Pelinovsky, Rogue waves in the basin of intermediate depth and the possibility of their formation due to the modulational instability, JETP Lett. **97**, 194 (2013).
[36] Z. Hu, H. Xue, W. Tang, and X. Zhang, Numerical study of nonlinear Peregrine breather under finite water depth, Ocean Eng. **108**, 70 (2015).
[37] G. Clauss, M. Klein, and M. Onorato, Formation of extraordinarily high waves in space and time, in *Proc. 30th Intel. Conf on Ocean, Offshore and Arctic Eng., June 19–24, 2011, Rotterdam, the Netherlands* (OMAE, 2011), pp. 1–13.
[38] E. A. Kuznetsov, Solitons in a parametrically unstable plasma, Sov. Phys. Dokl. **22**, 507 (1977).

[39] Y. C. Ma, The perturbed plane wave solutions of the cubic nonlinear Schrödinger equation, Stud. Appl. Math. **60**, 43 (1979).
[40] A. Chabchoub, B. Kibler, J. M. Dudley, and N. Akhmediev, Hydrodynamics of periodic breathers, Phil. Trans. R. Soc. A. **372**, 20140005 (2014).
[41] H. D. Zhang, G. Ducrozet, M. Klein, and C. G. Soares, An experimental and numerical study on breather solutions for surface waves in the intermediate water depth, Ocean Eng. **133**, 262 (2017).
[42] B. Liao, Y. Ma, X. Ma, and G. Dong, Experimental study on the evolution of Peregrine breather with uniform-depth adverse currents, Phys. Rev. E **97**, 053102 (2018).
[43] C. C. Mei, *The Applied Dynamics of Ocean Surface Waves* (World Scientific, Singapore, 1989).
[44] V. E. Zakharov and A. B. Shabat, Exact theory of two-dimensional self-focusing and one-dimensional self modulation of waves in nonlinear media, Sov. Phys. JETP. **34**, 62 (1972).
[45] D. H. Peregrine, Water waves, nonlinear Schrödinger equations and their solutions, J. Austral. Math. Soc. Ser. B. **25**, 16 (1983).
[46] H. Segur, D. Henderson, J. Carter, J. Hammack, C. Li, D. Pheiff, and K. Socha, Stabilizing the Benjamin-Feir instability, J. Fluid Mech. **539**, 229 (2005).
[47] Y. Ma, G. Dong, M. Perlin, X. Ma, and G. Wang, Experimental investigation on the evolution of the modulation instability with dissipation, J. Fluid Mech. **711**, 101 (2012).
[48] F. Ursell, The long wave paradox in the theory of gravity waves, Proc. Cambridge Philos. Soc. **49**, 685 (1953).
[49] A. R. Osborne and M. Petti, Laboratory-generated, shallow-water surface waves: Analysis using the periodic, inverse scattering transform, Phys. Fluids **6**, 1727 (1994).
[50] J. T. Kirby and R. A. Dalrymple, An approximate model for nonlinear dispersion in monochromatic wave propagation models, Coastal Eng. **9**, 545 (1986).
[51] M. L. Banner, X. Barthelemy, F. Fedele, M. Allis, A. Benetazzo, F. Dias, and W. L. Peirson, Linking Reduced Breaking Crest Speeds to Unsteady Nonlinear Water Wave Group Behavior, Phys. Rev. Lett. **112**, 114502 (2014).
[52] L. Shemer and B. K. Ee, Steep unidirectional wave groups-fully nonlinear simulations vs. experiments, Nonlinear Proc. Geophys. **22**, 737 (2015).
[53] Y. Ma, G. Dong, M. Perlin, X. Ma, G. Wang, and J. Xu, 2010 Laboratory observations of wave evolution, modulation and blocking due to spatially varying opposing currents, J. Fluid Mech. **661**, 108 (2010).
[54] C. Kharif, J.-P. Giovanangeli, J. Touboul, L. Grare, and E. Pelinovsky, Influence of wind on extreme wave events: Experimental and numerical approaches, J. Fluid Mech. **594**, 209 (2008).
[55] Yu. V. Sedletsky, The modulational instability of Stokes waves on the surface of finite-depth fluid, Phys. Lett. A **343**, 293 (2005).
[56] Y. Ma, X. Ma, M. Perlin, and G. Dong, Extreme waves generated by modulational instability on adverse currents, Phys. Fluids **25**, 114109 (2013).
[57] B. Liao, G. Dong, Y. Ma, and J. L. Gao, Linear-shear-current modified Schrödinger equation for gravity waves in finite water depth, Phys. Rev. E **96**, 043111 (2017).
[58] A. Slunyaev, E. Pelinovsky, A. Sergeeva, A. Chabchoub, N. Hoffmann, M. Onorato, and N. Akhmediev, Super-rogue waves in simulations based on weakly nonlinear and fully nonlinear hydrodynamic equations, Phys. Rev. E **88**, 012909 (2013).
[59] M. Onorato and D. Proment, Approximate rogue wave solutions of the forced and damped nonlinear Schrödinger equation for water waves, Phys. Lett. A **376**, 3057 (2012).
[60] D. M. Henderson, H. Segur, and J. D. Carter, Experimental evidence of stable wave patterns on deep water, J. Fluid Mech. **658**, 247 (2010).
[61] E. Lo and C. C. Mei, A numerical study of water-wave modulation based on higher-order nonlinear Schrödinger equation, J. Fluid Mech. **150**, 395 (1985).